# Role of Multiple Charge States of Ce in the Scintillation of ABO_{3} Perovskites

G. Pilania, S. K. Yadav, M. Nikl, B. P. Uberuaga, and C. R. Stanek

Phys. Rev. Applied **10**, 024026 — Published 20 August 2018

DOI: 10.1103/PhysRevApplied.10.024026

# Role of Multiple Charge States of Ce in the Scintillation of $ABO_3$ Type Perovskites

G. Pilania*
*Materials Science and Technology Division, Los Alamos National Laboratory, Los Alamos, NM 87545,USA*

S. K. Yadav
*Materials Science and Technology Division, Los Alamos National Laboratory, Los Alamos, NM 87545,USA and Metallurgical and Materials Engineering Department, Indian Institute of Technology Madras, Chennai, 600036, India*†

M. Nikl
*Institute of Physics, Academy of Sciences of the Czech Republic, 16253 Prague, Czech Republic*

B. P. Uberuaga
*Materials Science and Technology Division, Los Alamos National Laboratory, Los Alamos, NM 87545, USA*

C. R. Stanek
*Materials Science and Technology Division, Los Alamos National Laboratory, Los Alamos, NM 87545, USA*
(Dated: July 8, 2018)

Ce-activated $A^{2+}B^{4+}O_3$ perovskites represent a class of compounds currently under active exploration for their potential as scintillators. Depending on the chemistry and synthesis conditions, perovskites can crystallize in multiple crystal structures and a Ce substitutional dopant in an $ABO_3$ perovskite can adopt different charge states (*i.e.*, $Ce^{3+}$ or $Ce^{4+}$) as well as different substitutional sites (namely the 12-fold coordinated A-site or the octahedrally coordinated B-site). Here, we use first-principles density functional theory (DFT) and hybrid functional based computations to study relative trends in structure, energetics and electronic structure of bulk $ABO_3$ perovskites, where A = Ca, Sr and Ba and B = Hf and Zr. Subsequently, we consider the relative energetics of preferential solution sites for Ce as a function of charge states, chemical potential and defect configurations. Our results reveal that while $Ce^{3+}$ or $Ce^{4+}$ defects can be thermodynamically stable, depending on the choice of the substitutional site and synthesis conditions (*i.e.*, prevailing chemical potential), only $Ce^{3+}$ dopant at the A-site leads to an electronic structure that can exhibit scintillation. Our comparative analysis shows that while the positions of $5d^1$ and $4f$ levels of $Ce^{3+}$ doped at the A-site are favorably placed in the band structure, these levels are consistently higher for the $Ce^{4+}$ charge state and are unlikely to manifest any luminescence. Findings of the present study are also discussed in relation to previously reported results and display an excellent agreement with past experimental observations. In general, it is demonstrated that controlling Ce charge state and local chemical environment can be used — in addition to band gap and band edge engineering — to manipulate the relative position of scintillating states with respect to valence band maximum (VBM) and and conduction band minimum (CBM). While the the present study specifically focused on perovskites, the results (in particular, the relative alignment of the positions of $5d^1$ and $4f$ levels of Ce dopant as a function of the activator's charge state) are expected to be general and thus transferable to other chemistries.

## I. INTRODUCTION

Scintillators constitute an important class of materials that can efficiently absorb radiation and emit light pulses with a wavelength in or near the visible spectral region [1]. Inorganic scintillators are heavily employed in many fields of applied and fundamental research including radiation and particle detection in high-energy and astro-physics experiments, medical imaging, oil-well logging, and nuclear materials detection for homeland security [2–6]. High quality single crystals (*i.e.*, structurally perfect crystals with very low defect concentrations) of semiconductor or insulator materials are ideally suitable for these applications. In addition to a suitable bandgap, the materials must exhibit salient electronic structure features that allow for a fast and efficient transformation of incoming high energy radiation into a number of electron-hole pairs and their subsequent fast radiative recombination after being recollected at the conduction and valence band edges, respectively [6–8]. In many cases, owing to very high melting temperatures exhibited by these chemistries, synthesis of high quality single crystals becomes challenging and therefore other formats such as transparent polycrystalline ceramics are sought. While most of the past efforts related to transparent ceramic scintillators have explored binary halides [9–11], garnets [12], and ortho- and pyro-silicates [13, 14], more recent studies have focused on perovskites [15, 16]. In particu-

* gpilania@lanl.gov
† Current affiliation

lar, $A^{2+}B^{4+}O_3$ perovskite oxides with A ∈{Ca, Sr, Ba} and B ∈{Zr, Hf} and $A'^{3+}B'^{3+}O_3$ with A' ∈{Y, Gd, Lu} and B' ∈{Al} doped with Ce as an activator impurity have been investigated owing to their excellent gamma ray attenuation resulting from their high density and high effective atomic number [17–21]. Despite the significant efforts, however, only a limited amount of success has been achieved in making Ce-doped perovskites scintillating. In most cases no scintillating behavior is reported and the absence of scintillation is generally attributed to Ce $5d$ states buried deep in the conduction band, as a result of which excited electrons, after thermally relaxing to the conduction band edge, fail to localize at the luminescence centers.

More recently, however, a number of studies have reported radioluminescence performance in $BaHfO_3$ and $SrHfO_3$ based phosphors and scintillators when synthesized in special conditions [22–25]. These investigations have mainly relied on strategies such as (i) co-doping with various charge compensating metal ions such as Lu, Al, and Ta [22] or Li [23]; (ii) via heavy A-site doping of Ce in a highly A-deficient non-stoichiometric perovskite [24] or (iii) by synthesizing the compounds in highly reducing conditions [25]. However, mechanistic details of scintillation in these compounds across diverse chemistries are complicated due to a number of factors and have not yet been completely understood. For instance, for a given set of chemistries (*i.e.*, the choice of A and B atomic species) and synthesis conditions (*e.g.*, oxidizing or reducing conditions or excess of AO or $BO_2$ precursors), a Ce substitutional dopant in an $ABO_3$ perovskite can adopt different charge states (*i.e.*, $Ce^{3+}$ or $Ce^{4+}$) as well as different substitutional sites (*i.e.*, the 12-fold coordinated A-site or the 6-fold coordinated B-site). Thermodynamics of the dopant formation at different sites in different charge states is primarily governed by the prevailing chemical potential during the synthesis. The details of electronic structure — largely dictating the scintillation performance — are also closely and sensitively tied to the charge states and coordination environment of the activator. A systematic understanding of concerted interplay of these factors not only provides insight into the reported experimental observations but also opens new pathways towards a rational design of targeted functionality in these compounds.

First-principles calculations within the framework of density functional theory (DFT) and *'beyond'* approaches can be particularly useful in studying systematic trends and gaining insights into chemical and electronic properties of materials, and thereby aid the search for better materials or improved modifications of existing materials. In fact, over the past decade, DFT has been extensively employed to study and search for novel and improved rare-earth-doped inorganic scintillator materials and has already significantly contributed to our present understanding of these materials [17, 26–34]. The main aim of the present study is to understand trends in thermodynamic stability of Ce dopants within the perovskite crystal structure across a range of chemistries as a function of Ce charge state, doping site and synthesis conditions. Once the energetically favorable dopant sites and charge states are identified, the scintillation behavior can be qualitatively understood by looking at the relevant electronic structure features of the most energetically stable dopants. Towards this direction, here we study the relative thermodynamic stability of different doping situations as a function of chemical potential within the framework of first principles thermodynamics — an approach that has been extensively employed to study temperature and environment-dependent stability of bulk and surfaces phases within DFT. Further, since a necessary condition for scintillation in Ce-activated materials is that the Ce $4f$ and $5d^1$ levels must lie in the forbidden gap of the host material, appropriately situated with respect to the valence band maximum (VBM) and and conduction band minimum (CBM), our electronic structure analysis specifically focuses on the Ce $4f$ and $5d$ levels relative to the valence and conduction band edges.

A number of past studies have focused on $5d$-$4f$ transitions for a range of lanthanide activators using band-structure calculations [32–37]. A general consensus appears to be that for conventional local and semi-local exchange correlation functionals within DFT, such as the local-density approximation (LDA) or the generalized gradient approximation (GGA), the self-interaction error associated with the localized nature of the $4f$ electrons prohibits the calculation of accurate energy differences as well as the location of the energy bands. There have been attempts to overcome this problem either by using methods that go beyond DFT [30, 33] or by performing electronic-structure calculations with the LDA+U or GGA+U approach [38, 39] to get a better description of the localized $4f$ states of Ce compared to LDA or GGA [32, 34, 37]. However, it is needless to emphasize that care should be taken while approximating the exact $4f$-$5d$ excitation energies by the one-electron energies within the DFT framework. Using a combination of the pseudopotential plane-wave method along with the relativistic molecular orbital approach, Watanabe and coworkers [40] have studied the $4f$-$5d$ absorption spectra of Ce-doped $LiYF_4$. They concluded that owing to the simple $[Xe]4f^1$ electronic structure of $Ce^{3+}$ the $4f$-$5d$ transitions can indeed be attributed to transitions between molecular orbitals, and therefore can be analyzed within the framework of a single-electron approximation.

In the present study, we employ the hybrid Heyd-Scuseria-Ernzerhof (HSE) [41, 42] functionals that are built from the Perdew, Burke, and Ernzerhof (PBE) [46] GGA functional by replacing a fraction $\alpha$ of the semilocal PBE exchange interaction by a screened nonlocal functional (with a second parameter $\omega$ representing the inverse screening length) to investigate electronic structure of bulk and Ce-doped $ABO_3$ perovskites, where A = Ca, Sr and Ba and B = Hf and Zr. We find that the standard HSE06 functional (where the tuple $\{\alpha, \omega\}$ maps

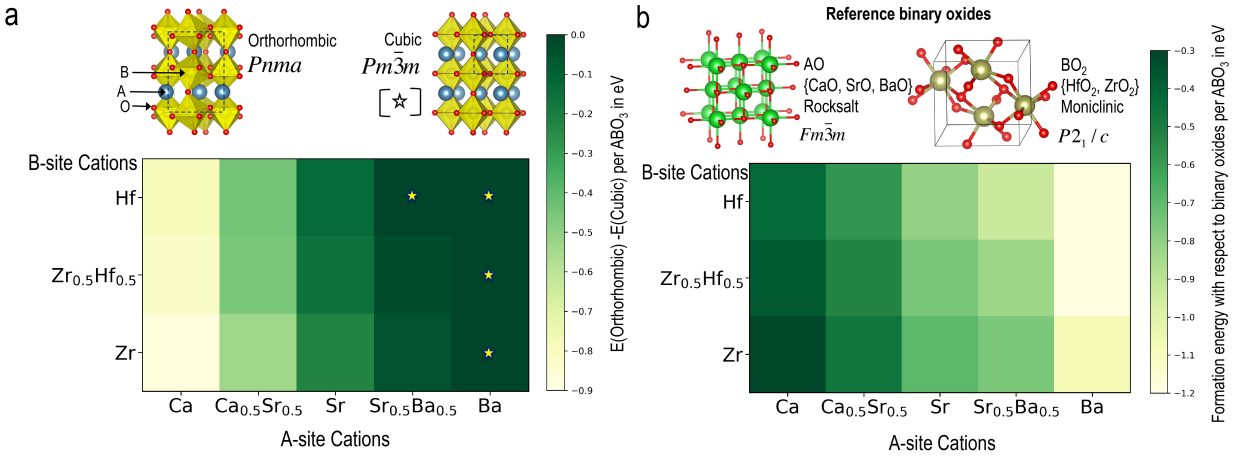


FIG. 1. (a) DFT energies per $ABO_3$ unit for different chemistries in the orthorhombic *Pnma* structure, computed relative to the the cubic $Pm\bar{3}m$ structure, reported as a function of A- and B-site chemistry. The two structures are also depicted on top of the matrix plot. The compounds that adopt the cubic $Pm\bar{3}m$ structure as the ground state are indicated with a '⋆'. (b) DFT formation energies of the $ABO_3$ perovskite compounds, computed in the most stable crystal structure identified in panel (a), *i.e.*, using either *Pnma* or $Pm\bar{3}m$, computed with respect to the corresponding ground state rocksalt AO ($Fm\bar{3}m$ space group) and monoclinic $BO_2$ ($P2_1/c$ space group) binary oxide phases. The unit cells used for the reference binary phases are presented at the top of the panel.

onto {0.25, 0.207 $Å^{-1}$}) [43], although representing a substantial improvement over the PBE results, still significantly underestimates the bulk bandgaps of the perovskite compounds. Further increasing $\alpha$ systematically leads to wider bandgaps. We show that tuning of $\alpha$ to reproduce the correct experimental bandgap for one of the bulk compounds not only reproduces the bulk bandgaps of rest of the compounds to a good accuracy, but also provides a correct description of their relative valence and conduction band alignments. This hybrid functional was subsequently used to compute the electronic structure of the Ce-doped supercells.

To summarize our results, our chemical-potential dependent dopant formation energies indicate that, depending on the experimental synthesis conditions, a Ce impurity can occupy substitutional sites at either A or B sub-lattices with +3 and +4 charge states, respectively. Substitutions with $Ce^{3+}$ at the B site and $Ce^{4+}$ at the A site consistently lead to higher formation energies, irrespective of the host chemistry. Furthermore, the A-site substituted $Ce^{3+}$ impurity is predicted to exhibit a scintillating behavior, while, for the $Ce^{4+}$ case, Ce $5d$ states always appear deep in the conduction band. Finally, consistent with the experimental observations, we predict that for both AO-deficient and highly reducing conditions, the A-site substituted $Ce^{3+}$ impurity is thermodynamically favorable as compared to the $Ce^{4+}$ substitution at the B-site, rationalizing the observed scintillating behavior in these specific situations. In what follows, we describe our findings in greater detail.

## II. TECHNICAL DETAILS

Density functional theory (DFT) calculations were performed using the Vienna *Ab initio* Simulation Package (VASP) [44, 45]. Unless mentioned otherwise, the DFT calculations employed the Perdew, Burke, and Ernzerhof (PBE) [46] generalized gradient approximation (GGA) exchange-correlation functional. The electronic wave functions were expanded in plane waves up to a cut-off energy of 500 eV. The pseudopotentials based on the projector augmented wave method [47] explicitly included following valence electronic configurations for different elemental species; Ce: $5s^25p^66s^24f^15d^1$, Ca: $3s^23p^64s^2$, Sr: $4s^24p^65s^2$, Ba: $5s^25p^66s^2$, Zr: $4p^64d^25s^2$, Hf: $5p^65d^26s^2$ and O: $2s^22p^4$. It is important to include the $4f$ shell as a part of Ce valence to allow for the 3+ charge state. A Gamma-centered automatically generated 4×4×3 Monkhorst-Pack $k$-point mesh [48] was used for Brillouin-zone integrations for a $\sqrt{2} \times \sqrt{2} \times 2$ cubic (or pseudo-cubic, in case of orthorhombic *Pnma* space group) supercell containing 20 atoms. For smaller or larger supercells, the $k$-point meshes were appropriately scaled to give the same $k$-point density in the reciprocal space. Spin-polarized calculations were employed for supercells containing unpaired electrons. To obtain a geometry optimized equilibrium structure, atomic positions, and the supercell lattice parameters were fully relaxed using the conjugate gradient method until all the Hellmann-Feynman forces and the stress component were less than 0.01 V/Å and $1.0\times10^{-2}$ GPa, respectively.

Sufficiently large supercells, containing 160 atoms, were consistently used to model the defect configurations. In the defect calculations, the dimensions of the

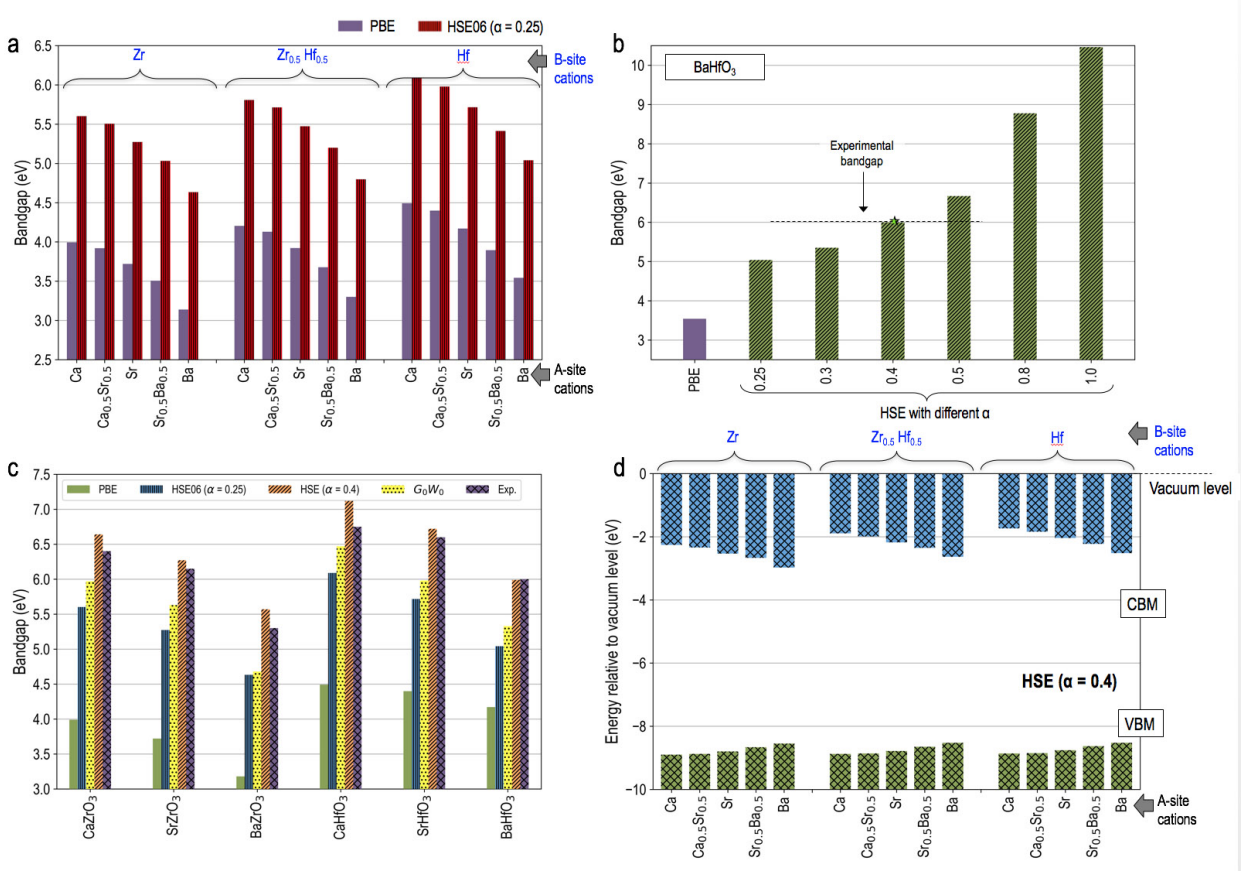


FIG. 2. (a) Bandgaps computed using the PBE and HSE06 functionals for the bulk single and double perovskites in their respective ground state crystal structures. Clear trends in the computed bandgaps as a function of A- and B-site chemistries can be seen. (b) Tuning of the bandgap for cubic $BaHfO_3$ perovskite by systematically varying the fraction of exact exchange $\alpha$ in the HSE hybrid functional. The experimental value of the bandgap, indicated by the horizontal dashed line, is achieved at $\alpha = 0.4$. The corresponding PBE value is also shown for comparison. (c) A comparison of the bandgaps, for the ground state structures of the six single $ABO_3$ perovskite chemistries, computed using different levels of theories employed in this study and corresponding experimentally reported values in the literature. (d) Relative valence and conduction band edge alignments for the perovskites computed within the HSE hybrid functional with $\alpha = 0.4$ as a function of A- and B-site chemistries. The zero of the energy corresponds to the vacuum level. The O 1s core levels were used to align the band edges relative to each other.

supercells were always fixed to the corresponding relaxed bulk lattice parameters, while all the internal degrees of freedom were allowed to relax. To model isolated Ce dopants in different charge states, electrons were adequately added or removed from the supercell and a compensating background charge density was added. Spurious electrostatic interactions of charged defects due to periodicity and finite supercell sizes were accounted for via first-order monopole corrections [49].

Since the conventional local and semi-local exchange correlation functional, including the PBE functional, are well known to significantly underestimate the electronic bandgap, the HSE functional was used on the relaxed PBE geometries to obtain an improved description of the bandgap and the activator's $4f$ and $5d^1$ levels. The hybrid density functional methods have been shown to improve results on the bandgap and charge localization in semiconductors and insulators [50–52]. However, we also note that for metallic systems the hybrid functionals are not suitable and have been reported to significantly overestimate bandwidths and exchange splitting [50].

Within this family of functionals, one has access to the parameters $\alpha$ and $\omega$, representing the fraction of exact exchange and the inverse screening length, respectively, that can be used to tune the details of electronic structure within a given class of materials. In particular, tuning of bandgaps, band edges and defect levels have been studied in detail [53]. For specific choices of the parameters $\{\alpha, \omega\}$ the standard functionals such as PBE $\{\alpha{=}0\}$, PBE0 $\{\alpha{=}0,\ \omega{=}0.207\ \text{Å}^{-1}\}$, and HSE06 $\{\alpha{=}0.25,\ \omega{=}0.207\ \text{Å}^{-1}\}$ can be obtained from the family of hybrid functionals. Kosma *et al.* have studied details of tuning the bandgap by varying $\alpha$ in PBE0-like (*i.e.*, $\omega$ fixed at 0) and in HSE-like (*i.e.*, $\omega$ fixed at 0.207 $\text{Å}^{-1}$) hybrid functionals [53]. Their results show that for PBE0-like functionals the bandgap increases linearly

with the fraction fraction of exact exchange $\alpha$, which is also in agreement with other reports [54, 55]. For HSE-like functionals, slight deviations from the linear behavior were observed and the change in the bandgap with the $\alpha$ occurs at a smaller rate. Going to non-standard hybrid functionals by further decreasing the screening lengths (*i.e.*, larger $\omega$), requires increasingly large fraction of exact exchange to reach to a given value of the bandgap. However, for such large values of $\alpha$, eventually lead to a poor description of energetics [41, 56]. It was also found that, when the band gap is tuned by varying $\alpha$, both PBE0 and HSE functionals yield nearly identical results for defect level positions in the band gap and for band offsets at interfaces. Following this approach, here we vary the amount of exact exchange $\alpha$ within the HSE-like functionals to tune the bandgaps in the perovskite compounds. As mentioned briefly in the introduction, we find that while the standard HSE06 functional [43] with $\alpha$ = 0.25 and $\omega = 0.207$ Å$^{-1}$, underestimates the bandgaps as compared to experiments, further increasing $\alpha$ to 0.4 and keeping the inverse screening length fixed to that of the standard HSE06 functional accurately reproduces the experimental bandgaps and the relative alignments of the band edges for the bulk compounds studied here. The HSE functional with $\alpha$ to 0.4 was subsequently used to study the electronic structure of the Ce-doped compounds.

## III. RESULTS

### A. Bulk Properties

Although the general focus of this work is the electronic structure and energetics of $Ce^{3+}$ or $Ce^{4+}$ doped $A^{2+}B^{4+}O_3$ perovskites with A = Ca, Sr or Ba and B = Hf or Zr, there are noteworthy structural differences and chemical trends among the bulk compounds considered. From a scintillation point of view, while the $A^{2+}B^{4+}O_3$ perovskite host compounds studied here consistently show high stopping power (owing to the high nuclear charge) and high melting temperatures, there are also tradeoffs in certain structure property relationships exhibited by these compounds. For instance, both $BaHfO_3$ and $BaZrO_3$ adopt cubic crystal structures with indirect bandgaps, whereas the other four compounds with Ca and Sr at the A-site, are orthorhombic direct bandgap insulators. Note, however, that a cubic material with a direct bandgap is ideally suitable as a scintillator host since with non-cubic materials its relatively difficult to produce large size transparent ceramics at a low cost, owing to their highly anisotropic nature. However, energy transfer from VBM to CBM has to be mediated with phonons in case of an indirect bandgap material. Therefore, before presenting our results on charge state and chemical potential dependent Ce dopant formation energies and substitutional site (*i.e.*, A- or B-sites) dependent electronic structure, we briefly discuss the structure, energetics and chemical trends in the bandgap and band-edges of bulk $A^{2+}B^{4+}O_3$ compounds.

The main structural distinction among the considered class of compounds is that, as already alluded to above, the compounds comprised of Ba at the A-site are cubic and crystallize in the $Pm\bar{3}m$ space group (No. 221) [57], while those with Ca or Sr at the A-site display and orthorhombic crystal structure with *Pnma* space group (No. 62) [62], owing to an energetically favored pattern of $BO_6$ octahedral rotations (*i.e.*, the $a^-b^+a^-$ tilt pattern configuration according to Glazer's notation) [58]. These local rotational distortions are driven due to the difference in ionic radius between $A^{2+}$ and $B^{4+}$ cationic species, and are generally described by the well known Goldschmidt *tolerance factor (t)* that aims to capture deviation from an idealized packing of cations and anions at the AO and $BO_2$ [001] planes in the structure [59]. The situation with $t = 1$ corresponds to an ideal perovskite while a decreasing $t$ corresponds to an increasing degree of distortion. Indeed the compounds considered in this study adhere to standard tolerance factor guidelines, *i.e.*, if the tolerance factor of a compound is near unity, that compound should be cubic (as is the case for $BaHfO_3$ and $BaZrO_3$, with $t$ = 1.009 and 1.004, respectively), and as the tolerance factor decreases the tendency for orthorhombic distortions to occur increases systematically [60–62].

To quantify the relative tendency for different chemistries to adopt cubic versus orthorhombic structure, we report the relative formation energy of the two phases as a function of A- and B-site chemistry in Fig. 1a. To better capture the chemical trends in energetics and electronic structure, in addition to the six bulk $ABO_3$ single perovskites, we also include chemistries formed by a 50% admixtures of rocksalt ordered A- and/or B-site cation pairs appearing as nearest neighbors in different columns of the Periodic Table. As can be seen from Fig. 1a, all compounds with Ba as the A-site cation as well as $Ba_{0.5}Sr_{0.5}HfO_3$ prefer the cubic $Pm\bar{3}m$ structure over the orthorhombic *Pnma* structure. As one moves to chemistries that exhibit either a smaller average A-site cation radius (going from Ba to Ca) and/or a larger average B-site cation radius (*i.e.*, going from Hf to Zr; note that the octahedrally coordinated $Zr^{4+}$ has a larger ionic radii than $Hf^{4+}$), the tendency for the B-site octahedral rotations increases, and as a result the orthorhombic crystal structure increasingly becomes more energetically favored. The relaxed lattice parameters for the bulk compounds in their respective ground state crystal structures are provided in the Table I and compared with available experimentally reported values. Note that a systematic overestimation of the structural parameters can be attributed to a well known tendency for a slight underbinding in the PBE functional, or in general for all GGA functionals, within DFT.

In addition to the relative formation energies between the cubic and orthorhombic phases, Fig. 1b reports the formation energies of the perovskite compounds (com-

TABLE I. DFT computed relative energies (energies computed in the orthorhombic $Pnma$ structure relative to the the cubic $Pm\bar{3}m$ structure), formation energies, relaxed bulk lattice parameters in the ground state structure and bandgaps computed at different levels of theory for the six $ABO_3$ single perovskites studied here. Reported experimental values for the lattice parameters and the bandgaps are also provided for comparison.

| $ABO_3$ | Space group | $E_{Pnma} - E_{Pm\bar{3}m}$ | $\Delta E_f$ | Lattice | | | Bandgap (eV) | | | | |
|---|---|---|---|---|---|---|---|---|---|---|---|
| Compound | Symbol | (eV/$ABO_3$) | (eV/$ABO_3$) | parameters (in Å) | | | PBE | HSE06 | $HSE_{\alpha=0.4}$ | $G_0W_0$ | Exp. |
| $CaZrO_3$ | $Pnma$ | -0.873 | -0.312 | 5.62 | 5.78 | 8.06 | 3.99 | 5.60 | 6.64 | 5.97 | (6.40)[e] |
| | | | | (5.59)[a] | (5.76)[a] | (8.02)[a] | | | | | |
| $SrZrO_3$ | $Pnma$ | -0.223 | -0.693 | 5.80 | 5.87 | 8.25 | 3.72 | 5.27 | 6.27 | 5.63 | (6.15)[e] |
| | | | | (5.79)[b] | (5.82)[b] | (8.20)[b] | | | | | |
| $BaZrO_3$ | $Pm\bar{3}m$ | 0.000 | -1.075 | 4.23 (4.19)[c] | | | 3.14 | 4.63 | 5.57 | 4.68 | (5.30)[f] |
| $CaHfO_3$ | $Pnma$ | -0.791 | -0.424 | 5.60 | 5.76 | 8.02 | 4.49 | 6.09 | 7.12 | 6.47 | (6.75)[e] |
| | | | | (5.57)[d] | (5.73)[d] | (7.98)[d] | | | | | |
| $SrHfO_3$ | $Pnma$ | -0.130 | -0.808 | 5.76 | 5.84 | 8.21 | 4.17 | 5.72 | 6.72 | 5.98 | (6.60)[e] |
| | | | | (5.78)[d] | (5.80)[d] | (8.18)[d] | | | | | (6.50)[g] |
| $BaHfO_3$ | $Pm\bar{3}m$ | 0.000 | -1.180 | 4.20 (4.18)[d] | | | 3.54 | 5.04 | 5.99 | 5.33 | (6.00)[h] |

**Experimental lattice parameters**: [a]Ref. [84], [b]Ref. [85], [c]Ref. [86], and [d]Ref. [60].
**Experimental bandgaps**: [e]The values are based on spectroscopic data combined with estimated exciton binding energies reported in Ref. [83], [f]Ref. [87], [g]Ref. [88], and [h]Ref. [89].

puted in the most stable crystal structure *i.e.* $Pnma$ or $Pm\bar{3}m$) with respect to the corresponding AO (*viz.* CaO [66], SrO [67] and BaO [68] in the rocksalt $Fm\bar{3}m$ crystal structure) and $BO_2$ (*viz.* $ZrO_2$ [69] and $HfO_2$ [70] in the monoclinic $P2_1/c$ crystal structure) binary phases. It is interesting to note the correlation between the relative energies in Fig. 1a and the formation energies in Fig. 1b, indicating that the larger the deviation from an idealized packing of cations and anions, the higher the extent of octahedral distortions to accommodate the size mismatch between the A- and B-site cations and the less stable the compound with respect to its binary constituents.

The correlation between the energies in Fig. 1a and Fig. 1b can also be understood by noting the fact that the formation enthalpy of a ternary oxide from the binary constituent oxides can generally be interpreted in terms of factors related to electron transfer between the two oxides, which intern depend on basic/acidic nature (or donor/acceptor quality) of the binary oxides. The larger the difference in acidity/basicity of AO and $BO_2$ is, the more exothermic the formation enthalpy becomes. While the alkaline earth metal oxides are usually basic, the transition metal oxides are acidic and the basicity increases when going down a specific group, for instance, as CaO < SrO < BaO (as the atomic radius of the metal ion increases. Note, however, again the exception due to the lanthanide contraction that leads to a larger ionic radii for Zr than Hf and therefore rendering $ZrO_2$ slightly more basic relative to $HfO_2$. In agreement with these general arguments, the formation energy of the ternary Ba oxides (from their binary constituents) are more negative than the corresponding Sr oxides that subsequently are more negative than the Ca oxides. Also, for any given A site cation, the formation energies of the ternary hafnates are more negative than the zirconates. Further, this trend between the acidity/basicity and the atomic radii of the metal cations is directly responsible for the observed correlation between the energies reported in Figs. 1a and b, via the Goldschmidt tolerance factor, as discussed above. We also note that the formation energies computed in this study are in good agreement with previously reported experimental [71–73] and theoretical results [74, 75]. The computed energies are provided in Table I.

Next we discuss the electronic structure, bandgaps and relative band edge positions of the bulk compounds. In agreement with previous reports, the electronic band structure and density of states of the $ABO_3$ compounds reveal that the valence bands are mainly constituted by O-2$p$ orbitals, while the B-atoms' $d$ orbitals largely contribute to the conduction bands. Those compounds stable in the cubic phase exhibit an indirect bandgap (with VBM and CBM laying at the R-point and Γ-point, respectively) while those stable in the orthorhombic phase have a direct bandgap at the Γ-point, this again is in agreement with previous findings. While the relative chemical trends in the bandgaps are expected to be correct within PBE, the actual bandgap values are grossly underestimated as compared to the experimentally measured ones. In fact, this is well known tendency for the local and semi-local exchange correlation functional within DFT (including the PBE functional employed here) which has been attributed to the inherent lack of derivative discontinuity [76] and delocalization error [77, 78] within the local or semi-local exchange-correlation functionals [79].

To obtain better predictions of the bandgaps, we resorted to more accurate (and also much more com-

putationally expensive) methods, namely, the hybrid HSE06 functional and single-shot quasiparticle GW (*i.e.*, $G_0W_0$)[80] calculations on top of the relaxed PBE geometry and PBE eigenfunctions. Figure 2a, compares our results of the bandgaps computed using the PBE and HSE06 functionals for the bulk perovskites in their respective ground state crystal structures. Indeed the bandgaps computed using the semi-local and hybrid exchange correlations functionals exhibit a very similar trend. In fact, the HSE06 bandgaps can simply be given by a linear function of the PBE bandgaps $\epsilon^{\mathrm{PBE}}$ as: $1.085\ \epsilon^{\mathrm{PBE}} + 1.2215$, to a very good accuracy (with a goodness of fit value $R^2 = 0.997$). Nevertheless, a comparison with corresponding experimental values (*cf.* Table I) reveals that the HSE06 bandgaps — though representing a significant improvement as compared to the PBE bandgaps — are still considerably underestimated. The bandgaps computed using the $G_0W_0$ calculations provide further improvements over the HSE06 values, however, still systematically lower than the experimental values, as can be seen from Fig. 2 and Table I. We also find that the relative trends that we see here for the HSE06 and the $G_0W_0$ bandgap calculations (with respect to experiments) are quite general and have also been reported for other wide bandgap materials [81, 82].

It has also been demonstrated previously that going beyond the single-shot GW method, via adopting the $GW_0$ approach, further improves the bandgap predictions [82]. In the $GW_0$ approach, the eigenvalues in the Green's function G are updated, whereas the screening properties are only calculated in the random-phase approximation using the PBE wave functions and eigenvalues. While accurate, this strategy is significantly more computationally expensive and not practical for large supercells containing defects/dopants. Alternatively, we explored a more *pragmatic* strategy, where we systematically vary the fraction of the Hartree-Fock exact exchange $\alpha$ in the DFT hybrid functional (while fixing the inverse screening length $\omega$ to that of the standard HSE06 value) to track the corresponding variation in the bangap. Figure 2b presents our results for $BaHfO_3$, where a value of $\alpha = 0.4$ reproduces the experimental bandgap. More interestingly, the bulk bandgaps computed with the HSE functional with $\alpha = 0.4$ for the rest of the compounds result in an excellent agreement with the corresponding experimental bandgap values at a much lower computational cost than the GW approach. In what follows, we consistently used the the HSE functional with $\alpha = 0.4$ to study electronic structure of the Ce doped perovskites, as discussed in Sec. III C

Finally, we note that within our hybrid functional approach, previously reported relative chemical trends for the valence and conduction band edges are also well captured [83]. To reliably determine the relative position of band edges in compounds, a reference state that does not change with chemical composition first needs to be identified. While there are several schemes available in the literature [31, 90–93], we use the binding energy of oxygen $1s$ core electrons to calculate relative positions of the valence and conduction band edges. An experimentally reported value of the valence band edge for $BaZrO_3$ with respect to the vacuum level from ref. [83] then allows us to pin the zero of energy. The binding energy of the oxygen $1s$ core electrons is calculated as the energy difference between two separate calculations.[94, 95] The first calculation is a standard DFT calculation in which the number of core electrons corresponds to the ground state whereas for the second calculation one electron is removed from the core of one particular atom and added to the valence or conduction band. The energy difference then provides the core-level binding energy. Note that the core electron binding energies can be calculated in either the initial state approximation or the final state approximation. In the final state approximation the electrons are allowed to relax after the core electron has been removed, so that the acquired localized hole is screened. In the initial state approximation, on the other hand, the core electron is removed but no change of the potential (*e.g.*, by relaxing other electrons) is allowed and electronic screening is therefore entirely neglected. The oxygen core $1s$ level, however, is sufficiently deep and we don't expect the predicted values from the two approximations to differ considerably. Further, since the core electron binding energy in the initial state approximation can be calculated directly from the Kohn-Sham eigenvalues of the core states and the Fermi level, this approximation was used here to compute the oxygen $1s$ core levels. We also note here that in past $2s$ state of oxygen has been used as a reference to align band edges in garnets [31]. With the deep core state identified, the band edges of the bulk perovskites then can be compared directly by shifting the band structure of one with respect to the others such that the deep state energy levels coincide across chemistries.

Figure 2d presents our results on the relative conduction and valence band edge alignments for different chemistries in a stacked band scheme. It can be seen in Fig. 2d that there are systematic variations in the relative band edge alignments, which closely follow chemical trends in the periodic table. As we go down group 2 of the periodic table (from Ca to Ba) atomic size as well as the metallic nature increase and the bandgap systematically decreases. Both the lowering of the CBM and rise in the VBM contribute to the bandgap reduction, although the changes in the CBM position are greater than those in the VBM position. Unlike the A-site atomic species, Zr and Hf have a very similar atomic radii and chemical nature, as a result only relatively small changes in the band edge alignment with respect to the B-site atomic species are evident. Finally, we note that the computed trends are in close agreement with experimental observations [83].

### B. Charge State and Chemical Potential Dependent Defect Energetics

The $A^{2+}B^{4+}O_3$ perovskite compounds explored here typically display high melting points and are also frequently employed in formats other than single crystals such as transparent polycrystalline ceramics [25, 96] and nanocrystals [23, 97]. While a range of intrinsic defects (such as cation antisite and anion vacancies) – as dictated by thermodynamics at finite temperatures – can naturally occur in these materials, extrinsic defects can also be formed; for instance, via non-stoichiometry or from aliovalent activators through charge compensation (*e.g.*, in case of $Ce^{3+}$). The presence of defects can have a strong effect on the underlying electronic structure, including the features that are critical to scintillation performance. For instance, in the Ce-activated $BaHfO_3$ ceramics, a strong influence of the preparation atmosphere (reducing, oxidizing, or inert) on the scintillation efficiency has been reported [25]. Also, contrary to the conventional belief that $SrHfO_3$ is a line compound in the composition-temperature phase diagram, a small non-stoichiometry in terms of Zr-excess has been reported [98] and Sr-vacancies have been proposed as defects related to $SrHfO_3$ nonstoichiometry [24]. Nikl *et al.* recently synthesized heavily Ce-doped $SrHfO_3$ and undoped non-stoichiometric $SrHfO_3$ [24]. Interestingly, they not only found a new emission band at about 334 nm in Sr-deficient sample, but also demonstrated a room temperature decay time of about 180 ns and efficient and fast energy transfer from the host to the center of the 334 nm emission. Loureiro *et al.* synthesized Ce-activated $BaHfO_3$ and $SrHfO_3$ perovskites with different charge compensating co-dopants [22]. They found that $Ce^{3+}$ doping at the A-site is much easier in $SrHfO_3$ than in $BaHfO_3$. In fact, high $Ce^{3+}$ doping concentrations in a $BaHfO_3$ host lattice were only stabilized at very high temperatures and in reducing conditions, where as for $SrHfO_3$ it was found that higher relative percentages of $Ce^{3+}$ at the Sr-site could be obtained at much milder conditions. In addition, the site preference of lanthanide activators has important optical property implications, as charge transfer is reduced with increasing both the nearest-neighbor distance between the activator and oxygen ions [99] and the coordination number [100]. The site preferences of $Tm^{3+}$ in $SrHfO_3$ [101], Eu in $BaHfO_3$ [102], and Eu in $SrZrO_3$ nano phosphors [103] have been examined in the past.

In addition to the conventional $Ce^{3+}$ centers, a new and exciting avenue is presented by recent developments on scintillation performance improvement by luminescent $Ce^{4+}$ centers in Ce-doped oxides, in particular garnets [30, 104, 105] and orthosilicates [106]. A $Ce^{4+}$ center, if stable in these oxides, can provide an additional fast radiative recombination pathway since it can efficiently compete with any electron traps for an immediate capture of electrons from the conduction band. In contrast, a $Ce^{3+}$ center is much less effective in this competition since it first needs to capture a hole from the valence band to be able to capture an electron in a subsequent step. Also note that scintillation through $Ce^{3+}$ and $Ce^{4+}$ centers in a material can, in principle, work in parallel and therefore the two centers do not compete but rather complement each other. As a result, presence of stable $Ce^{4+}$ centers, with appropriately placed electronic levels in the host bandgap, can positively influence several scintillation characteristics, including light yield, speed of scintillation response and afterglow. Indeed acceleration of scintillation response in alkaline earth metal co-doped $Lu_3Al_5O_{12}$:Ce and $Lu_{1.95}Y_{0.05}SiO_5$:Ce has been attributed to the presence of $Ce^{4+}$ centers in recent reports [30, 104–106].

Stanek and co-workers [17] have reported a systematic study of defect chemistry in $A^{2+}B^{4+}O_3$ perovskite compounds (with $A^{2+} = Ba^{2+}$ or $Sr^{2+}$, and $B^{4+} = Zr^{4+}$ or $Hf^{4+}$) employing both atomistic calculations using potentials and DFT computations. This study examined a range of intrinsic defect reactions, several situations with A and B excess non-stoichiometry and a number of possible reactions for $M^{3+}$ rare earth cation doping, $Lu^{3+}$ to $La^{3+}$. While for the stoichiometric cases a Schottky disorder was predicted to be the lowest energy intrinsic process, for non-stoichiometric situations with AO-excess ($BO_2$-excess) a charge compensation mechanism by oxygen vacancies (by A vacancies) was found to be the most energetically favored. For the $M^{3+}$ dopant formation energies, the following specific reactions were considered (using the Kröger–Vink notation [108]):

$$M_2O_3 + 3A_A^{\times} \Leftrightarrow 2M_A^{\bullet} + V_A^{''} + 3AO, \tag{1a}$$

$$M_2O_3 + 2B_B^{\times} + O_O^{\times} \Leftrightarrow 2M_B^{'} + V_O^{\bullet\bullet} + 2BO_2, \tag{1b}$$

$$M_2O_3 + 2A_A^{\times} + B_B^{\times} \Leftrightarrow 2M_A^{\bullet} + A_B^{''} + ABO_3, \tag{1c}$$

$$M_2O_3 + 2A_A^{\times} + B_B^{\times} \Leftrightarrow 2M_B^{'} + B_A^{\bullet\bullet} + ABO_3, \tag{1d}$$

$$M_2O_3 + 2A_A^{\times} + B_B^{\times} \Leftrightarrow 2M_i^{\bullet\bullet\bullet} + V_A^{''} + V_B^{''''} + ABO_3. \tag{1e}$$

While some of these reactions have also previously been considered by others [107], this comprehensive investigation showed that not only the preferred reaction sensitively depends on the specific $M^{3+}$ dopant being considered, but also that the formation energies can vary by several eV across these reactions for a given dopant. For $Ce^{3+}$ doping cases, however, A-site was consistently favored for the entire set of compounds with reaction (1a) being the most energetically favored route.

Despite all of these studies, there are a number of questions — with particular relevance for scintillators — that remain to be answered regarding Ce doping in $ABO_3$ perovskites. In particular, questions such as "*What is the site preference and dopant formation energy for the $Ce^{4+}$ charge state*?" and "*How does it compare with that of the $Ce^{3+}$ charge state*?" remain to be answered. Also, perhaps more importantly, "*How do these formation energies and site-preferences change with respect to chem-*

TABLE II. Ce dopant formation energies as a function of Ce charge state and substitutional site, according to reactions given in Eq. 2 and computed for the two extreme limits of the allowed chemical potential ranges as per Eq. 3 for the different A- and B-site chemistry. For each case, two different situations — where defects (*i.e.*, Ce and the corresponding charge compensating defect) are modeled in either a clustered or in isolated configurations — are considered. The most favorable defect formation energies at the two extreme chemical potential limits are highlighted in **bold** for each $ABO_3$ compound. See text for details.

| | | | Defect formation energies | | | |
|---|---|---|---|---|---|---|
| | | | AO-poor conditions | | AO-rich conditions | |
| Perovskite | Eq. | Ce Doping | Isolated defects | Clustered defects | Isolated defects | Clustered defects |
| $CaHfO_3$ | (2a) | $Ce_{Ca}^{+3}$ | **0.26** | 0.40 | 0.92 | 1.06 |
| Ortho- | (2b) | $Ce_{Hf}^{+3}$ | 3.11 | 1.93 | 2.67 | 1.49 |
| rhombic | (2c) | $Ce_{Ca}^{+4}$ | 1.17 | 1.47 | 2.05 | 2.35 |
| *Pnma* | (2d) | $Ce_{Hf}^{+4}$ | 1.19 | N/A | **0.76** | N/A |
| $CaZrO_3$ | (2a) | $Ce_{Ca}^{+3}$ | **0.12** | 0.40 | 0.60 | 0.88 |
| Ortho- | (2b) | $Ce_{Zr}^{+3}$ | 2.37 | 1.62 | 2.05 | 1.29 |
| rhombic | (2c) | $Ce_{Ca}^{+4}$ | 0.90 | 1.36 | 1.56 | 2.01 |
| *Pnma* | (2d) | $Ce_{Zr}^{+4}$ | 0.84 | N/A | **0.52** | N/A |
| $SrHfO_3$ | (2a) | $Ce_{Sr}^{+3}$ | **-0.23** | 0.27 | 1.04 | 1.53 |
| Ortho- | (2b) | $Ce_{Hf}^{+3}$ | 2.63 | 1.81 | 1.79 | 0.97 |
| rhombic | (2c) | $Ce_{Sr}^{+4}$ | 0.72 | 1.37 | 2.41 | 3.05 |
| *Pnma* | (2d) | $Ce_{Hf}^{+4}$ | 0.92 | N/A | **0.07** | N/A |
| $SrZrO_3$ | (2a) | $Ce_{Sr}^{+3}$ | **-0.52** | 0.21 | 0.56 | 1.30 |
| Ortho- | (2b) | $Ce_{Zr}^{+3}$ | 1.70 | 1.83 | 0.97 | 1.10 |
| rhombic | (2c) | $Ce_{Sr}^{+4}$ | 0.23 | 1.14 | 1.68 | 2.60 |
| *Pnma* | (2d) | $Ce_{Zr}^{+4}$ | 0.43 | N/A | **-0.29** | N/A |
| $BaHfO_3$ | (2a) | $Ce_{Ba}^{+3}$ | **0.67** | 0.93 | 2.51 | 2.77 |
| Cubic | (2b) | $Ce_{Hf}^{+3}$ | 2.81 | 1.84 | 1.58 | 0.62 |
| $Pm\bar{3}m$ | (2c) | $Ce_{Ba}^{+4}$ | 2.40 | 2.23 | 4.85 | 4.68 |
| | (2d) | $Ce_{Hf}^{+4}$ | 1.12 | N/A | **-0.10** | N/A |
| $BaZrO_3$ | (2a) | $Ce_{Ba}^{+3}$ | **0.64** | 1.01 | 2.33 | 2.70 |
| Cubic | (2b) | $Ce_{Zr}^{+3}$ | 1.91 | 1.53 | 0.79 | 0.41 |
| $Pm\bar{3}m$ | (2c) | $Ce_{Ba}^{+4}$ | 2.31 | 2.08 | 4.56 | 4.33 |
| | (2d) | $Ce_{Zr}^{+4}$ | 0.73 | N/A | **-0.39** | N/A |

*ical environment (i.e., with systematic variations in the chemical potential)*?" has not been addressed. In the remainder of this section, we address these issues in a systematic manner and interpret available experimental observations in light of our computational results.

Building on previous work [17], here we consider the most stable reactions found for the $Ce^{3+}$ doping at the A- and B-sites, respectively. In addition, we also consider two analogous reactions for $Ce^{4+}$ doping. These are depicted below. For $Ce^{3+}$ doping at the A and B crystal sites we have:

$$Ce_2O_3 + 3A_A^{\times} \Leftrightarrow 2Ce_A^{\bullet} + V_A^{''} + 3AO, \quad (2a)$$

$$Ce_2O_3 + 2B_B^{\times} + O_O^{\times} \Leftrightarrow 2Ce_B^{'} + V_O^{\bullet\bullet} + 2BO_2, \quad (2b)$$

and for $Ce^{4+}$ doping at the A and B crystal sites the relevant reactions are:

$$CeO_2 + 2A_A^{\times} \Leftrightarrow Ce_A^{\bullet\bullet} + V_A^{''} + 2AO \quad (2c)$$

$$CeO_2 + B_B^{\times} \Leftrightarrow Ce_B + BO_2. \quad (2d)$$

Note that either bulk AO or bulk $BO_2$ appears in each of the above reactions. While its is a common practice to use respective bulk enthalpies (or DFT total energies) as chemical potentials (*i.e.*, $\mu_{AO} = E_{AO}^{Bulk}$ and $\mu_{BO_2} = E_{BO_2}^{Bulk}$) to evaluate 0 K defect formation energies, the thermodynamic equilibrium conditions during the $ABO_3$ bulk formation strictly require the condition $\mu_{AO} + \mu_{BO_2} = \mu_{ABO_3} = E_{ABO_3}^{Bulk}$ to follow and therefore $\mu_{AO}$ and $\mu_{BO_2}$ can not vary independently. Further, if the system contains an excess of AO, the excess AO may form a bulk AO precipitate. Consequently, the chemical potential of AO may not exceed the chemical potential of bulk AO; $\mu_{AO} \leqslant E_{AO}^{Bulk}$. Similarly, the chemical potential of $BO_2$ may not exceed that of bulk $BO_2$; $\mu_{BO_2} \leqslant E_{BO_2}^{Bulk}$. In other words, the following bounds on the chemical potentials $E_{ABO_3}^{Bulk} - E_{BO_2}^{Bulk} \leqslant \mu_{AO} \leqslant E_{AO}^{Bulk}$ or equivalently $E_{ABO_3}^{Bulk} - E_{AO}^{Bulk} \leqslant \mu_{BO_2} \leqslant E_{BO_2}^{Bulk}$ have to be enforced.

Therefore, to compute the formation energy of the above reactions as a function of chemical potential, we conveniently define two extreme chemical potential limits, namely the *AO-rich* and the *AO-poor* conditions. Specifically, for the *AO-rich* conditions we have,

$$\mu_{AO} = E_{AO}^{Bulk} \quad (3a)$$

$$\mu_{BO_2} = E_{ABO_3}^{Bulk} - E_{AO}^{Bulk}. \quad (3b)$$

On the other hand, for the *AO-poor* conditions the two limiting chemical potentials are given by:

$$\mu_{AO} = E_{ABO_3}^{Bulk} - E_{BO_2}^{Bulk} \quad (3c)$$

$$\mu_{BO_2} = E_{BO_2}^{Bulk}. \quad (3d)$$

Note that the *AO-rich* and the *AO-poor* limits map on to the *$BO_2$-poor* and the *$BO_2$-rich* limits, respectively, and beyond these limits, a bulk $ABO_3$ perovskite phase will be thermodynamically unstable with respect to decomposition into its binary oxides. The chemical potential within these limits can be varied by either directly changing the concentrations of AO and $BO_2$ or indirectly *via* controlling the chemical potential of oxygen (oxidizing or reducing conditions). Finally, we note that at extreme reducing conditions, it may also be possible to reduce the binary metal oxides to their respective metallic phases and gaseous oxygen. In that case the chemical potential definitions need to be suitably modified to include

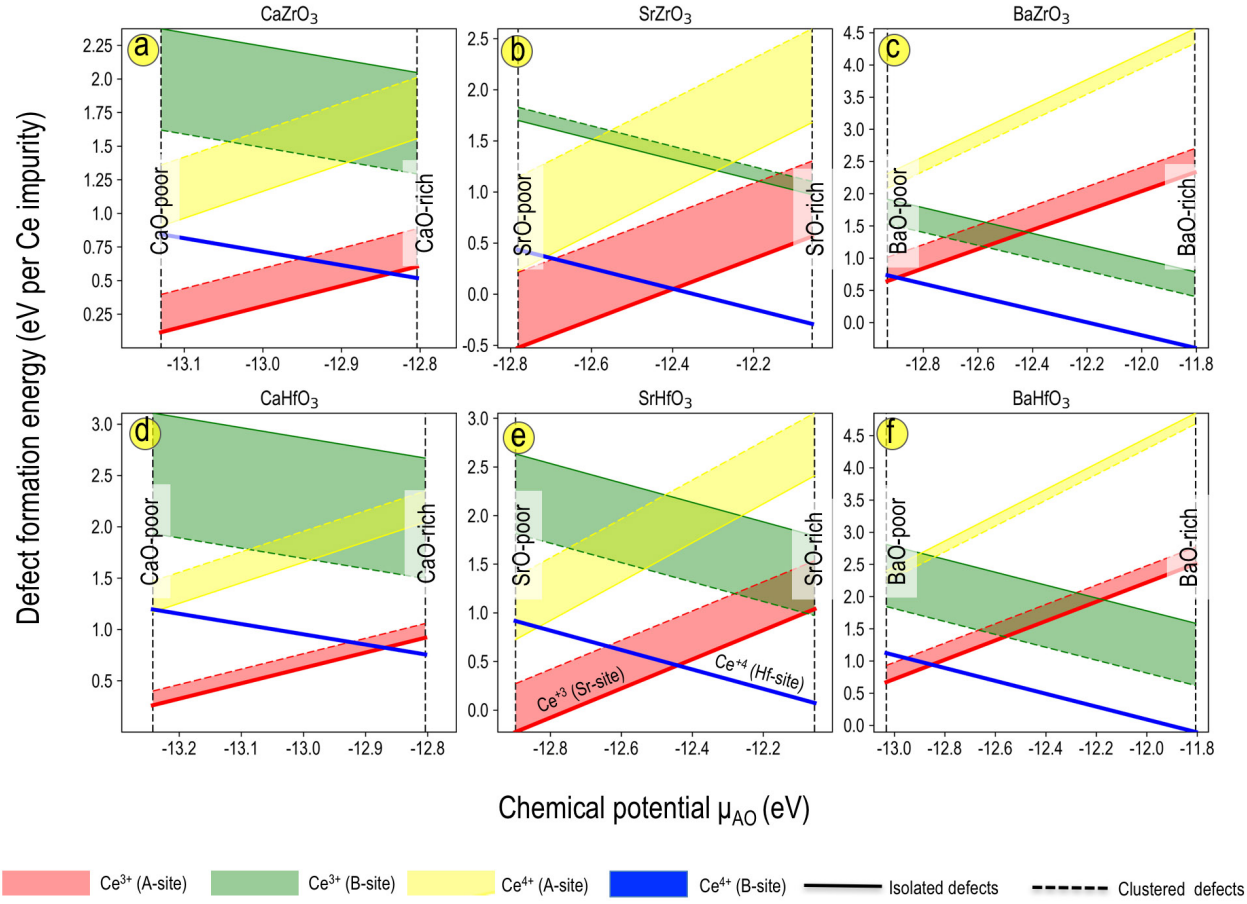


FIG. 3. Chemical potential dependent Ce dopant formation energies computed as a function of the Ce charge state (*i.e.*, 3+ or 4+) and the substitutional sites (*i.e.*, the A or B cation site) in the respective ground state structures of the $ABO_3$ perovskites. In each case, the energy range covered by different possible configurations of the defect clusters is highlighted with different color fills and the solid and dashed lines represent the two extreme cases where the defect clusters are modeled in isolated or closely clustered configurations, respectively. The two extreme (*i.e.*, the AO-poor and AO-rich) chemical potential limits are given as per Eq. 3.

also the energetics of the bulk metallic phases. However, in the present analysis we have neglected such extreme reducing conditions.

In Table II, we report the computed DFT (PBE) formation energies at the two extreme chemical potential limits for the four reactions given in Eq. 2 for each of the six bulk single perovskites chemistries considered here. Further, for each case we have considered two different scenarios where the Ce dopant and the associated charge compensating defect (if applicable) are clustered at the nearest possible lattice sites or are isolated. For the former case, the dopant and the defect were modeled in the same supercell, whereas for the later each defect was modeled in different supercells separately.

Figure 3 graphically presents the results reported in Table II. Red, yellow, green and blue lines are used for $Ce_A^{3+}$, $Ce_A^{4+}$, $Ce_B^{3+}$, $Ce_B^{4+}$ doping situations, respectively. The solid lines represent the energetics for isolated defect configurations while the dashed lines are used for the clustered defect configurations. The area between each pair of the respective solid and dashed lines (depicting the energetics for the isolated and clustered defects) is filled, representing the expected variations in the computed defect energies due to relative positions of the Ce dopants and the associated charge compensating defects. It can be seen from the figure that irrespective of the chemistry the defect configurations with either $Ce^{3+}$ at the A site or $Ce^{4+}$ at the B site (depicted by red and blue lines and given by Eqs. 2a and 2d, respectively) consistently result in the lowest defect formation energies. On the other hand, doping situations with $Ce^{3+}$ at the B site and $Ce^{4+}$ at the A site always result in higher energies, irrespective the chemical potential. While the trends exhibited by zirconates and hafnates are qualitatively very similar, changing A-site chemistry from Ca to Sr to Ba results in a systematic variation in the defect energetics. For instance, the range of chemical potential for which $Ce_A^{3+}$ ($Ce_B^{4+}$) is predicted to be thermodynamically stable gradually decreases (increases) going from Ca to Ba

in both the zirconate and hafnate compounds.

### C. Electronic Structure of $Ce_A^{3+}$ and $Ce_B^{4+}$ Dopants

From the results presented in the previous section, it is clear that depending on the chemical potential (or synthesis conditions) $Ce^{3+}$ doping at the A-site (Eq. 2a) or $Ce^{4+}$ doping at the B-site (Eq. 2d) are the thermodynamically most favored cases for solution of Ce in $ABO_3$ perovskites. In this section, we compare qualitative details of the electronic structure between $Ce^{3+}$ doping at the A-site and $Ce^{4+}$ doping at the B-site, with an aim to understand and contrast their scintillation behavior in an $ABO_3$ host environment.

From an electronic structure point of view, a necessary condition for scintillation in Ce-doped materials is that both the Ce $4f$ and $5d$ levels must lie within the host bandgap and should also have suitable positions with respect to host valence and conduction band edges, respectively. The first is an absolutely necessary criterion for scintillation, while the second is critical for performance. If the Ce $4f$ ($5d$) level is buried in the valence (conduction) band of the host, then there will be no Ce-activated scintillation. On the other hand, a Ce $4f$ level that lies too high above the VBM is also not desirable, as it leads to a poor hole capture probability at the activator site. Furthermore, if the $Ce^{3+}$ excited state $(Ce^{3+})^*$ lies below but too close to the CBM, then thermal excitations from the $5d$ state into the conduction band can, in principle, reduce or even completely quench luminescence, thereby leading to a poor scintillator. Finally, too large of an energy difference in the CBM and the excited state level would also decrease the probability for the Ce ion to capture an electron since more phonon modes would need to be available to dissipate the large energy.

As a natural next step, we employ DFT computations to calculate the relative positions and associated charge densities of the Ce $4f$ and $5d$ states with respect to host valence and conduction band edges, respectively. Ce dopants with 3+ (for the A-site) and 4+ (for the B-site) charge states are modeled in a sufficiently large supercell (*i.e.*, a supercell that allows us to recover a bulk-like behavior away from the dopant) from periodically repeating the unit cell of the host crystal. We allow for relaxation of all the internal coordinates while keeping the cell dimensions fixed to that of the bulk. While for the B-site doping, Ce naturally adopts a +4 charge state and thus preserves the charge of the original B ion, one electron per Ce atom was removed from the supercell for the A-site doping situations and a neutralizing background charge was used for simulating the charged supercells and describing the 3+ charge state. We also note that the aim in these studies is to model an isolated Ce dopant in an infinite host crystal, however, in practice the finite supercell approach may introduce spurious dopant-dopant interactions due to the periodic boundary conditions which in turn result in a broadening of the impurity levels into bands. Although, filled and empty $4f$ levels — for $Ce^{3+}$ and $Ce^{4+}$ dopants, respectively — are typically atom-like and therefore highly localized, the bands associated with Ce-localized 5d states typically exhibit some dispersion due to finite-size effects as well as owing to some degree of hybridization with the host d-states forming the CBM. Despite these complications, the electronic structure analysis based on DFT computations can be practically useful in understanding the relative trends across chemistries, albeit in a qualitative manner.

To compare and contrast key differences in the electronic structure of the $Ce_A^{+3}$ and $Ce_B^{+4}$ dopants, Fig. 4 presents our results for total and partial density of states (DOS) and band decomposed charge density analyses for $CaHfO_3$ computed using hybrid DFT (*i.e.*, the HSE functional with $\alpha = 0.4$, as discussed in Sec. III A). Note that the presentation of $CaHfO_3$ is only for illustration, qualitatively similar results were obtained for the other $ABO_3$ compounds, as presented in the Supplemental Material [109].

Figures 4a–c present total and site-projected partial density of states (for Ce $4f$ and $5d$ states) for $Ce^{3+}$ doping at the Ca site. The Ce $4f$ state localizes within the bandgap ∼2.0 eV above the VBM and is singly occupied. This is further confirmed by plotting the total spin charge density for the supercell (which also exactly matches with the Ce $4f$ band decomposed charge density) shown in Fig. 4. As briefly discussed above, unlike the Ce $4f$ state, the $5d$ states are relatively more dispersed, owing to their hybridization with the Hf $5d$ states and form the bottom of the conduction band edge. A plot of the band decomposed charged density for the band associated with the CBM clearly shows that the density is largely localized on the Ce atom and the surrounding Hf atoms, alluding to a high probability of localization of an excited electron to the activator site upon relaxation to the conduction band edge.

While looking at the charge density associated with empty bands forming the conduction band edge is insightful, it is worthwhile to note that a ground-state calculation with the $4f$ level filled and the $5d$ level empty generally gives rise to a $5d$ level that will be higher in energy than when the $5d$ level is filled and the $4f$ level empty. This effect can be simply understood based on screening arguments. Since the $4f$ level is closer to the nucleus than the $5d$ level, a filled $4f$ level can effectively screen the $5d$ level from an attractive Coulombic interaction from the nucleus. However, when the $4f$ level is emptied, the screening effect from the positive nuclei will be reduced and the $5d$ level will relax to a lower energy. Therefore, from a mechanistic point of view it is more relevant to simulate an excited $5d$ level in $Ce^{3+}$ (*i.e.*, when the unpaired electron has been transferred from the $4f$ to the lowest $5d$ level of the dopant), also frequently denoted as $(Ce^{3+})^*$. However, an accurate determination of the Ce $5d$ level below the CBM in the $(Ce^{3+})^*$ state, in principle, requires many-body approaches beyond conventional DFT, which can be extremely challenging and

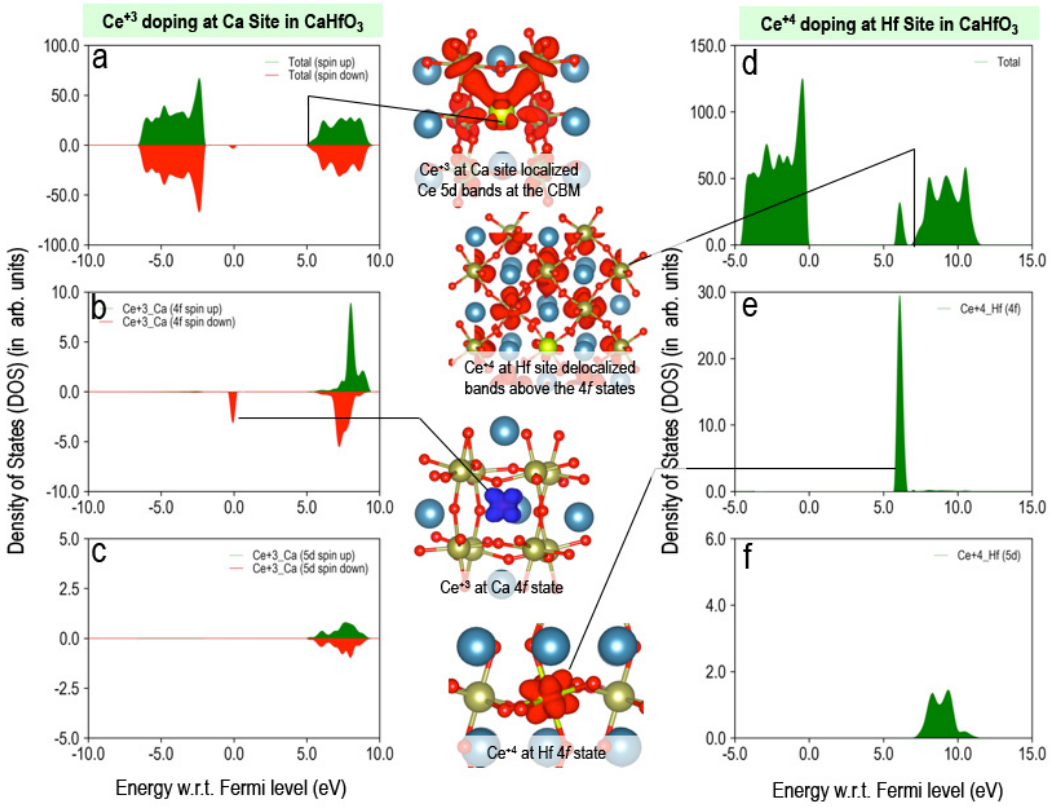


FIG. 4. Total and partial (Ce $4f$ and $5d$) density of states for the two most stable (depending on the chemical potential) Ce substitutional doping configurations in $CaHfO_3$, computed within the HSE hybrid functional with $\alpha = 0.4$. (a) Total, (b) Ce $4f$ and (c) Ce $5d$ states for a $Ce^{3+}$ dopant at the Ca site. Panels (d), (e) and (f) report the corresponding results for a $Ce^{4+}$ dopant at the Hf site. For the $Ce^{3+}$ dopant spin-up and spin-down states are colored in green and red, respectively. In each panel, zero of the energy correspond to the Fermi level. The central panels show the band decomposed charge density corresponding to the conduction band edges (the top two configurations) and the Ce dopants $4f$ states (the bottom two configurations) for supercells containing a $Ce^{3+}$ at the Ca site and a $Ce^{4+}$ dopant at the Hf site, respectively.

computationally demanding for large supercells. Alternately, we performed excited-state (constrained hybrid DFT) calculations to verify that the Ce $5d$ level does indeed lowers by about 0.6 eV with respect to the VBM in the $(Ce^{3+})^*$ excited state. Finally, we note that the Stokes shift can also be computed by allowing for lattice relaxation around the $(Ce^{3+})^*$ state, which further lowers the $5d$ level. However, previous studies have pointed out that the Stokes shift is difficult to model accurately with DFT-based band-structure calculations. Since here we aim towards a comparative qualitative understanding of the electronic structure of Ce as a function of charge state and substitutional site, we did not try to model Stokes shift explicitly in our simulations and the excited state was simulated without allowing for the geometric relaxation.

While the $Ce^{3+}$ dopant at the Ca site provides a favorable band structure in terms of the VBM–4f gap as well as a suitably localized 5d state near the CBM, details of the electronic structure for a $Ce^{4+}$ dopant at the Hf site — shown in Fig. 4 panels (d–f) — present a sharp contrast. Most prominently, the empty $4f$ level in the $Ce^{4+}$, still localized at the activator site, shifts towards a higher energy, widening the VBM-$4f$ charge transfer gap considerably. Furthermore, the 5d states in the $Ce^{4+}$ at the Hf site are predicted to be deeper, buried inside the conduction band. The CBM in this case is formed largely by the Hf $5d$ states which are fairly delocalized as can be seen from the band decomposed charge density associated with the conduction band edge plotted in Fig. 4. Therefore, unlike the $Ce^{3+}$ dopant at the Ca site, in this case both the 4f and the 5d levels of the Ce activator are unfavorably located in the bandgap as a result of which $Ce^{4+}$ dopant at the Hf site is highly unlikely to exhibit a scintillating behavior. Based on our analysis, this charge state dependence of the $4f$ and $5d$ levels for a Ce impurity — schematically depicted in Fig. 5 — is not specific to $CaHfO_3$ and is anticipated to be true, in general, for any $A^{2+}B^{4+}O_3$-type perovskite chemistry. In fact, We note that qualitatively similar charge state dependent shifts in the Ce levels have recently been reported both theoretically and experimentally in garnets [30].

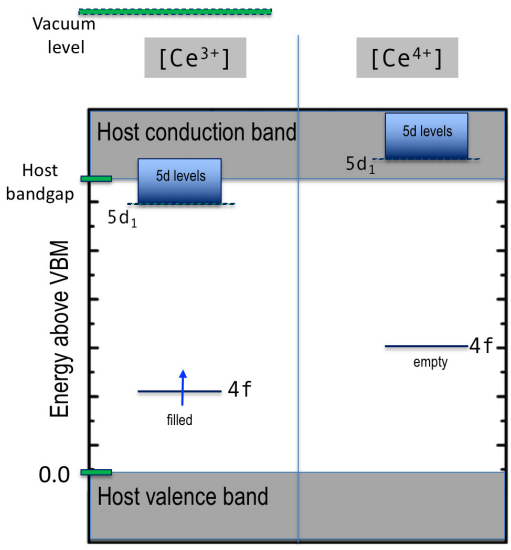


FIG. 5. A schematic representation of charge state dependence (*i.e.*, +3 *versus* +4) of the $4f$ and $5d$ levels for a Ce impurity in an $ABO_3$ host environment. Note that the comparison in the illustration is only meant for a qualitative understanding.

## IV. DISCUSSION AND CONCLUSIONS

While our theoretical investigation relies on a number of approximations/simplifications, as discussed in the previous section, to make the adopted computational methodology efficient, practical and tractable, it already provides useful insights into previously reported experimental observations. Most notably, our work demonstrates that the observed scintillating behavior of the $ABO_3$ compounds can be directly attributed to $Ce^{3+}$ charge state and the $Ce^{4+}$ state is incapable of acting as a luminescent center. This is in remarkable agreement with the fact that the experimental investigations that have reported radioluminescence performance in $ABO_3$ perovskites based phosphors and scintillators have mainly relied on strategies that tend to stabilize $Ce^{3+}$ charge state relative to the $Ce^{4+}$ state. For instance, co-doping with various charge compensating metal ions such as Lu, Al, and Ta [22] or Li [23] that lead to radioluminescence are naturally expected to favor the 3+ charge state for Ce. Furthermore, as evident by our chemical potential dependent defect formation energy analysis, heavy A-site doping of Ce in a highly A-deficient perovskite (*i.e.*, AO-poor) that results in a good luminescence performance would also favor $Ce^{3+}$ charge state at the A site [24]. Finally, the luminescence reported by synthesizing the compounds in highly reducing conditions [25] can also be understood by noting that the AO-poor condition actually allows for a lower lower-bound on the possible range of oxygen chemical potential and therefore favors a more reducing environment as compared to that of the AO-rich condition. More precisely, the bounds on the oxygen chemical potential can be written as $\mu_{AO} - \mu_A \leqslant \mu_O \leqslant 1/2\mu^{gas}_{O_2}$. Since, in the AO-poor conditions, $\mu_{AO}$ is always lower than that of the AO-rich conditions, this translates to a lower allowed bound for $\mu_O$ and therefore allowing for a more reducing condition. Our results for the Ce substitutional defect formation energies also correlate well with previously reported experimental observations. For instance, Loureiro *et al.* observed that a $SrHfO_3$ host lattice with higher relative percentages of $Ce^{3+}$ can be obtained at much milder conditions as compared to $BaHfO_3$ [22]. In close agreement with the experimental results, a comparison between the computed defect formation energies of $SrHfO_3$ and $BaHfO_3$ clearly shows lower formation energies and a wider stability range for $Ce^{3+}$ at the Sr site in $SrHfO_3$ as compared to $Ce^{3+}$ at the Ba site in $BaHfO_3$. Lastly, we note that the energy-level diagrams of $Ce^{3+}$ and $Ce^{4+}$ in $Gd_3Ga_3Al_2O_{12}$ garnet compound are recently established experimentally, which indicate a higher position of the $5d^1$ state of $Ce^{4+}$ in the forbidden gap in comparison to that of $Ce^{3+}$, again in qualitative agreement with the results obtained in our electronic structure analysis [30].

In summary, we used first-principles conventional DFT and hybrid functional computations to study (i) the relative trends in structure, energetics and electronic structure of bulk $ABO_3$ perovskites, (ii) relative energetics of preferential solution sites for Ce as a function of charge states, chemical potential and defect configurations in the Ce doped perovskites and (iii) electronic structure of the most stable Ce doping configurations (given by a combination of the preferred substitutional site and energetically favored charge state) identified as a function of the prevalent chemical potential was investigated by looking at the total and dopant's partial density of states as well as the band decomposed charge density analysis. Our computational results for the bulk perovskites compare favorably with previously reported experimental results and reconfirm well understood systematic chemical trends in structure, energetics and electronic structure across the targeted chemistries. Subsequently, our analysis for chemical potential dependent Ce substitutional dopant formation energies reveals that a $Ce^{3+}$ substitutional dopant is always favored at the A-site in a reducing environment, whereas a $Ce^{4+}$ substitutional defect is consistently favored at the B-site in an oxidizing environment. Further electronic structure analysis shows that while depending on experimental synthetic conditions both $Ce^{3+}$ at the A-site and $Ce^{4+}$ at the B-site can, in principle, be thermodynamically stable, only $Ce^{3+}$ at the A-site exhibits favorable electronic structure that can potentially support the experimentally observed scintillating behavior and the $Ce^{4+}$ charge state is unlikely to manifest any luminescence. Our results, although expected to be qualitative, are discussed in relation to previously reported experimental finding and display an excellent agreement with available experimental observations. In general, it is demonstrated that controlling charge state and substitutional sites of Ce could

be yet another way (in addition to band gap and band edge engineering) to manipulate the relative position of scintillating states with respect to valence and conduction band edges.

## ACKNOWLEDGMENTS

GP, BPU and CRS gratefully acknowledge support from Laboratory Directed Research and Development (LDRD) program within the Los Alamos National Laboratory (LANL) — an affirmative action equal opportunity employer operated by Los Alamos National Security, LLC, for the National Nuclear Security Administration of the U.S. DOE under Contract No. DEAC52-06NA25396. Computational support for this work was provided by LANL's high performance computing clusters.

[1] G. F. Knoll, Radiation Detection, and Measurement (Wiley, New York, 2010).
[2] G. Blasse, Scintillation materials, Chem. Mater. 6, 1465 (1994).
[3] P. A. Rodnyi, Physical Processes in Inorganic Scintillators (CRC Press, Boca Raton, 1997).
[4] M. J. Weber, Inorganic scintillators: Today and tomorrow, J. Lumin. 100, 35 (2002).
[5] M. Nikl and A. Yoshikawa, Recent R&D trends in inorganic single-crystal scintillator materials for radiation detection, Adv. Opt. Mater. 3, 463 (2015).
[6] Lecoq, Paul, Alexander Gektin, and Mikhail Korzhik, Inorganic scintillators for detector systems: physical principles and crystal engineering. Springer, 2016.
[7] P. A. Rodnyi, P. Dorenbos, and C. W. E. van Eijk, Energy Loss in Inorganic Scintillators, Phys. Stat. Sol. (b) 187, 15 (1995).
[8] M. Nikl, Scintillation detectors for x-rays, Meas. Sci. Technol. 17, R37 (2006).
[9] R. Hofstadter, The detection of gamma-rays with thallium-activated sodium iodide crystals, Phys. Rev. 75, 796 (1949).
[10] W. van Sciver, R. Hofstadter, Scintillations in Thallium-Activated $CaI_2$ and CsI, Phys. Rev. 84, 1062 (1951).
[11] K. W. Krämer, P. Dorenbos, H. U. Güdel, C. W. E. Van Eijk, Development and characterization of highly efficient new cerium doped rare earth halide scintillator materials, J. Mater. Chem., 16(27), 2773-2780 (2006).
[12] M. Nikl, A. Yoshikawa, K. Kamada, K. Nejezchleb, C. R. Stanek, J. A. Mares, K. Blazek, Development of LuAG-based scintillator crystals: a review, Prog. Cryst. Growth Charact. Mater. 59, 47 (2013).
[13] M. Nikl, A. Vedda, V. V. Laguta, Single-crystal scintillation materials, in Springer Handbook of Crystal Growth (Eds: G. Dhanaraj , K. Byrappa , V. Prasad , M. Dudley), Springer, Heidelberg 2010, 1663-1700.
[14] V. Jary, M. Nikl, S. Kurosawa, Y. Shoji, E. Mihokova, A. Beitlerova, G. P. Pazzi, A. Yoshikawa, Luminescence characteristics of the $Ce^{3+}$-doped pyrosilicates: The case of La-admixed $Gd_2Si_2O_7$ single crystals, J. Phys. Chem. C 118 , 26521 (2014).
[15] M. D. Birowosuto, D. Cortecchia, W. Drozdowski, K. Brylew, W. Lachmanski, A. Bruno, and C. Socib, X-ray Scintillation in Lead Halide Perovskite Crystals, Sci Rep. 2016; 6: 37254.
[16] T. Yanagida, Study of rare-earth-doped scintillators. Optical Materials, 35, 1987-1992 (2013).
[17] L. Casillas-Trujillo, D. A. Andersson, B. Dorado, M. Nikl, K. E. Sickafus, K. J. McClellan, and C. R. Stanek, Intrinsic defects, nonstoichiometry, and aliovalent doping of $A^{2+}B^{4+}O_3$ perovskite scintillators, Phys. Status Solidi B 251, 2279-2286 (2014).
[18] E. V. van Loef, W. M. Higgins, J. Glodo, A. Lempicki, V. Venkataramani, W. W. Moses, S. E. Derenzo, and K. S. Shah, Scintillation Properties of $SrHfO_3$:$Ce^{3+}$ and $BaHfO_3$:Ce $^{3+}$ Ceramics, IEEE Trans. Nucl. Sci. 54, 741-743 (2007).
[19] C. Michail, N. Kalyvas, I. Valais, S. David, I. Seferis, A. Toutountzis, A. Karabotsos, P. Liaparinos, G. Fountos, and I. Kandarakis, On the response of $GdAlO_3$:Ce powder scintillators, J. Lumin. 144, 45-52 (2013).
[20] W. Drozdowski, A. J. Wojtowicz, T. Lukasiewicz and J. Kisielewski, Scintillation properties of LuAP and LuYAP crystals activated with Cerium and Molybdenum. Nucl. Instr. Meth. Phys. Res. A 562, 254-261 (2006).
[21] A. J. Wojtowicz, J. Glodo, W. Drozdowski, and K. R. Przegietka, Electron traps and scintillation mechanism in $YAlO_3$: Ce and $LuAlO_3$: Ce scintillators. J. Lumin. 79, 275-291 (1998).
[22] Sergio M. Loureiro, Yan Gao, and Venkat Venkataramani, Stability of Ce(III) Activator and Codopant Effect in MHfO3 (M = Ba, Sr) Scintillators by XANES, J. Am. Ceram. Soc., 88, 219-221 (2005).
[23] Y.M. Ji, D.Y. Jiang, L.S. Qin, J.J. Chen, T. Feng, Y.K. Liao, Y.P. Xu, J.L. Shi, Preparation and luminescent properties of nanocrystals of $Ce^{3+}$-activated $SrHfO_3$, J. Cryst. Growth 280, 93, (2005).
[24] M. Nikl, P. Bohacek, B. Trunda, V. Jary, V. Studnicka, R. Kucerkova, and A. Beitlerova, SrHfO $_3$-based phosphors and scintillators, Opt. Mater. 34, 433-438 (2011).
[25] A. Grezer, E. Zych, and L. Kepinski, $BaHfO_3$: Ce sintered ceramic scintillators, Radiat. Meas. 45, 386-388 (2010).
[26] J. Andriessen, E. van der Kolk, and P. Dorenbos, Lattice relaxation study of the 4f-5d excitation of $Ce^{3+}$-doped $LaCl_3$, $LaBr_3$, and $NaLaF_4$: Stokes shift by pseudo Jahn-Teller effect, Phys. Rev. B 76, 075124 (2007).
[27] C. Ortiz, O. Eriksson, and M. Klintenberg, Data mining and accelerated electronic structure theory as a tool in the search for new functional materials, Comp. Mater. Sci. 44, 1042 (2009).
[28] W. Setyawan, R. M. Gaume, S. Lam, R. S. Feigelson, and S. Curtarolo, High-Throughput Combinatorial

Database of Electronic Band Structures for Inorganic Scintillator Materials, ACS Combinatorial Sci. 13, 382 (2011).
[29] M. Fasoli, A. Vedda, M. Nikl, C. Jiang, B. P. Uberuaga, D. A. Andersson, K. J. McClellan, and C. R. Stanek, Band-gap engineering for removing shallow traps in rare-earth $Lu_3Al_5O_{12}$ garnet scintillators using $Ga^{3+}$ doping, Phys. Rev. B 84, 081102(R) (2011).
[30] Y. Wu, F. Meng, Q. Li, M. Koschan, and C. L. Melcher, Role of $Ce^{4+}$ in the scintillation mechanism of codoped $Gd_3Ga_3Al_2O_{12}$:Ce. Phys. Rev. Applied 2, 044009 (2014).
[31] S. K. Yadav, B. P. Uberuaga, M. Nikl, C. Jiang, C. R. Stanek, Band-Gap and Band-Edge Engineering of Multicomponent Garnet Scintillators from First Principles, Phys. Rev. Applied 4, 054012 (2015).
[32] A. Canning, A. Chaudhry, R. Boutchko, and N. Grønbech-Jensen, First-principles study of luminescence in Ce-doped inorganic scintillators, Phys. Rev. B 83, 125115 (2011).
[33] K. Biswas and M.-H. Du, Energy transport and scintillation of cerium-doped elpasolite $Cs_2LiYCl_6$: Hybrid density functional calculations, Phys. Rev. B 86, 014102 (2012).
[34] A. Chaudhry, R. Boutchko, S. Chourou, G. Zhang, N. Grønbech-Jensen, and A. Canning, First-principles study of luminescence in $Eu_{2+}$-doped inorganic scintillators, Phys. Rev. B 89, 155105 (2014).
[35] L. Petit, A. Svane, Z. Szotek, and W. M. Temmerman, First-principles study of rare-earth oxides, Phys. Rev. B 72, 205118 (2005).
[36] M. Stephan, M. Zachau, M. Groting, O. Karplak, V. Eyert, K. Mishra, and P. Schmidt, A theoretical investigation of 4f-5d transition of trivalent rare earth ions in fluorides and complex oxides, J. Lumin. 114, 255 (2005).
[37] Y. Wu, Q. Li, S. Jones, C. Dun, S. Hu, M. Zhuravleva, A. C. Lindsey, L. Stand, M. Loyd, M. Koschan, J. Auxier II, H. L. Hall, and C. L. Melcher, Defect Engineering by Codoping in $KCaI_3$:$Eu^{2+}$ Single-Crystalline Scintillators, Phys. Rev. Applied 8, 034011 (2017).
[38] A. I. Liechtenstein, V. I. Anisimov and J. Zaane, First-principles calculations of the electronic structure and spectra of strongly correlated systems: the LDA+ U method, Phys. Rev. B 52, R5467 (1995).
[39] S. L. Dudarev, G. A. Botton, S. Y. Savrasov, C. J. Humphreys and A. P. Sutton, Electron-energy-loss spectra and the structural stability of nickel oxide: An LSDA+U study, Phys. Rev. B 57, 1505 (1998).
[40] S. Watanabe and K. Ogasawara, Experimental and First-Principles Analysis of 4f-5d Absorption Spectrum for $Ce_{3+}$ in $LiYF_4$ Considering Lattice Relaxation, J. Phys. Soc. Jpn. 77, 084702 (2008).
[41] J. Heyd, G. E. Scuseria, and M. Ernzerhof, Hybrid functionals based on a screened Coulomb potential, J. Chem. Phys. 118, 8207 (2003).
[42] J. P. Perdew, M. Ernzerhof, and K. Burke, Rationale for mixing exact exchange with density functional approximations, J. Chem. Phys. 105, 9982 (1996).
[43] A.V. Krukau, O. A. Vydrov, A. F. Izmaylov, and G. E. Scuseria, Influence of the exchange screening parameter on the performance of screened hybrid functionals, J. Chem. Phys. 125, 224106 (2006).
[44] G. Kresse and J. Furthmüller, Efficient iterative schemes for ab initio total-energy calculations using a plane-wave basis set, Phys. Rev. B 54, 11169 (1996).
[45] G. Kresse and D. Joubert, From ultrasoft pseudopotentials to the projector augmented-wave method, Phys. Rev. B 59, 1758 (1999).
[46] J. P. Perdew, K. Burke, and M. Ernzerhof, Generalized Gradient Approximation Made Simple, Phys. Rev. Lett. 77, 3865 (1996).
[47] P. E. Blöchl, Projector augmented-wave method, Phys. Rev. B 50, 17953 (1994).
[48] H. J. Monkhorst and J. D. Pack, Special points for Brillouin-zone integrations, Phys. Rev. B 13, 5188 (1976).
[49] G. Makov and M. C. Payne, Periodic boundary conditions in ab initio calculations, Phys. Rev. B 51, 4014 (1995).
[50] J. Paier, M. Marsman, K. Hummer, G. Kresse, I. C. Gerber, and J. G. Angyan, J. Chem. Phys. 124, 154709 (2006).
[51] C. C. Wang, G. Pilania, and R. Ramprasad, Dielectric properties of carbon-, silicon-, and germanium-based polymers: A first-principles study, Phys. Rev. B 87, 035103 (2013).
[52] A. Mannodi-Kanakkithodi, G. Pilania, T. D. Huan, T. Lookman and R. Ramprasad, Machine Learning Strategy for Accelerated Design of Polymer Dielectrics, Sci. Rep. 6, 20952 (2016).
[53] H.-P. Komsa, P. Broqvist, and A. Pasquarello, Alignment of defect levels and band edges through hybrid functionals: Effect of screening in the exchange term, Phys. Rev. B 81, 205118 (2010).
[54] P. Broqvist, A. Alkauskas, and A. Pasquarello, Defect levels of dangling bonds in silicon and germanium through hybrid functionals, Phys. Rev. B 78, 075203 (2008).
[55] A. Alkauskas, P. Broqvist, F. Devynck, and A. Pasquarello, Band offsets at semiconductor-oxide interfaces from hybrid density-functional calculations, Phys. Rev. Lett. 101, 106802 (2008).
[56] A. V. Krukau, O. A. Vydrov, A. F. Izmaylov, and G. E. Scuseria, J. Chem. Phys. 125, 224106 (2006).
[57] H. D. Megaw, Crystal structure of double oxides of the perovskite type, Proc. Phys. Soc. 58, 133 (1946).
[58] A. M. Glazer, The Classification of Tilted Octahedra in Perovskites, Acta Cryst. B28, 3384-3392 (1972).
[59] V. M. Goldschmidt, Die Gesetze der Krystallochemie, Naturwissenschaften 21, 477-485 (1926).
[60] A. Feteira, D. C. Sinclair, K. Z. Rajab, and M.T. Lanagan, Crystal Structure and Microwave Dielectric Properties of Alkaline Earth Hafnates, $AHfO_3$ (A= Ba, Sr, Ca) J. Am. Ceram. Soc. 91, 893-901 (2008).
[61] I. M. Reaney, E. L. Colla, and N. Setter, Dielectric and Structural Characteristics of Ba-Based and Sr-Based Complex Perovskites as a Function of Tolerance Factor, Jpn. J. Appl. Phys. 1, 3984 (1994).
[62] I. Levin, T. G. Amos, S. M. Bell, L. Farber, T. A. Vanderah, R. S. Roth, and B. H. Toby, Phase equilibria, crystal structures, and dielectric anomaly in the $BaZrO_3$?$CaZrO_3$ system, J. Solid State Chem. 175, 170?181 (2003).
[63] B. J. Kennedy, C. J. Howard, and B. C. Chakoumakos, High-temperature phase transitions in $SrHfO_3$, Phys. Rev. B 60, 2972?2975 (1999).
[64] C. J. Howard, K. S. Knight, B. J. Kennedy, and E. H. Kisi, The structural phase transitions in stron-

tium zirconate revisited, J. Phys.: Condens. Matter 12, L677?L683 (2000).
[65] A. Ahtee, M. Ahtee, A. M. Glazer, and A. W. Hewat, The structure of orthorhombic $SrZrO_3$ by neutron powder diffraction, Acta Crystallogr. B 32, 3243?3246 (1976).
[66] R. Ganguly, V. Siruguri, I. K. Gopalakrishnan and J. V. Yakhmi, Stability of the layered $Sr_3Ti_2O_7$ structure in $La_{1.2}$ $(Sr_{1-x}Ca_x)_{1.8}$ $Mn_2O_7$, J. Phys.: Condens. Matter, , 12, 1683 (2000).
[67] D. Taylor, Thermal expansion data. I: Binary oxides with the sodium chloride and wurtzite structures, MO., Trans. Brit. Ceram. Soc., 83, 5 (1984).
[68] L.-G. Lieu and W. A. Bassett, Effect of pressure on the crystal structure and the lattice parameters of BaO, J. Geophys. Res., 77, 4934 (1972).
[69] C. J. Howard, R. J. Hill and B. E. Reichert, Structures of $ZrO_2$ polymorphs at room temperature by high-resolution neutron powder diffraction, Acta Crystallogr., B44, 116 (1988).
[70] R. E. Hann, P. R. Suitch and J. L. Pentecost, Monoclinic Crystal Structures of $ZrO_2$ and $HfO_2$ Refined from X?ray Powder Diffraction Data, J. Am. Ceram. Soc., 68, 285 (1985).
[71] S. Stølen, in Experimental Thermodynamics, Volume VI: Measurement of the Thermodynamics Properties of Single Phases, ed. A. R. H. Goodwin, K. N. Marsh and W. A. Wakeham, Elsevier, Amsterdam, pp. 408-432 (2003).
[72] J. Gaudiakas, R. G. Haire and J. Fuger, J. Chem. Thermodyn., 22, 577 (1990).
[73] L. R. Morss, J. Less-Common Met., 93, 301 (1983).
[74] P. G. Sundell, M. E. Björketun and G. Wahnstro? m, Phys. Rev. B: Condens. Matter, 73, 104112 (2006).
[75] J.-R. Martinez, C. E. Mohn, S. Stølen and R. Søndena, What can a "quantum black-box" do for the inorganic thermochemist? Phys. Chem. Chem. Phys., 8, 2036-2039 (2006).
[76] L. J. Sham and M. Schlüter, *Density-functional theory of the energy gap*, Phys. Rev. Lett. **51**, 1888 (1983).
[77] A. J. Cohen, P. Mori-Sánchez, and W. Yang, *Fractional charge perspective on the bandgap in density-functional theory*, Phys. Rev. B **77**, 115123 (2008).
[78] P. Mori-Sánchez, A. J. Cohen, and W. Yang, *Localization and delocalization errors in density functional theory and implications for band-gap prediction*, Phys. Rev. Lett. **100**, 146401 (2008).
[79] R. M. Martin, *Electronic structure: Basic theory and practical methods*, Cambridge University Press (2004).
[80] M. S. Hybertsen and S. G. Louie, Electron correlation in semiconductors and insulators: Band gaps and quasiparticle energies, Phys. Rev. B 34, 5390 (1986).
[81] F. Tran, and P. Blaha, Accurate band gaps of semiconductors and insulators with a semilocal exchange-correlation potential, Phys. Rev. Lett. 102, 226401 (2009).
[82] M. Shishkin and G. Kresse, Self-consistent GW calculations for semiconductors and insulators, Phys. Rev. B 75, 235102 (2007).
[83] P. Dorenbos, The electronic structure of lanthanide doped compounds with 3d, 4d, 5d, or 6d conduction band states, J. Lumin. 151 224-228 (2014) .
[84] H. J. A. Koopmans, G. M. H. van de Velde and P. J. Gellings, Powder Neutron Diffraction Study of the Perovskites $CaTiO_3$ and $CaZrO_3$, Acta Cryst. C39, 1323-1325 (1983).
[85] Y. Zhao and D. J. Weidner, Thermal expansion of $SrZrO_3$ and $BaZrO_3$ perovskites, Phys. chem. minerals 18, 294-301 (1991).
[86] I. Charrier-Cougoulic, T. Pagnier, G. Lucazeau, Raman Spectroscopy of Perovskite-Type $BaCe_x$ $Zr_{1-x}O_3$ ($0 \leqslant x \leqslant 1$), J. Solid State Chem. 142, 220 (1999).
[87] J. J. Robertson, Band offsets of wide-band-gap oxides and implications for future electronic devices, Vac. Sci. Technol. B. 18, 1785-1791 (2000).
[88] D. J. Lee, Y. K. Seo, Y. S. Lee, and H. -J. Noh, Spectroscopic investigation on the electronic structure of a 5d band insulator $SrHfO_3$ in proximity to ferroelectric instability: Comparison with $SrTiO_3$ and $SrZrO_3$, Solid State Commun. 150, 301 (2010).
[89] C. Azahaf, H. Zaari, A. Abbassi, H. Ez-Zahraouy, and A. Benyoussef, Theoretical investigation of spontaneous polarization, electronic and optical properties of cubic perovskite $BaHfO_3$, Opt. Quant. Electron. 47, 2889-2897 (2015).
[90] S.-H. Wei and A. Zunger, Band offsets and optical bowings of chalcopyrites and Zn-based II-VI alloys, J. Appl. Phys. 78, 3846 (1995).
[91] P. G. Moses and C. G. Van deWalle, Band bowing and band alignment in InGaN alloys, Appl. Phys. Lett. 96, 021908 (2010).
[92] C. G. Van de Walle and R. M. Martin, Theoretical calculations of heterojunction discontinuities in the Si/Ge system, Phys. Rev. B 34, 5621 (1986).
[93] A. Franciosi and C. G. Van de Walle, Heterojunction band offset engineering, Surf. Sci. Rep. 25, 1 (1996).
[94] L. Köhler and G. Kresse, Density functional study of CO on Rh(111), Phys. Rev. B 70, 165405 (2004).
[95] S. Lizzit, A. Baraldi, A. Groso, K. Reuter, M. V. Ganduglia-Pirovano, C. Stampfl, M. Scheffler, M. Stichler, C. Keller, W. Wurth, and D. Menzel, Surface Core Level Shifts of Clean and Oxygen Covered Ru (0001), Phys. Rev. B 63, 205419 (2001).
[96] E. V. van Loef, Y. Wang, S. R. Miller, C. Brecher, W. H. Rhodes, G. Baldoni, S. Topping, H. Lingertat, V. K. Sarin, and K. S. Shah, Effect of microstructure on the radioluminescence and transparency of Ce-doped strontium hafnate ceramics, Opt. Mater. 33, 84-90 (2010).
[97] H. Retot, A. Bessiere, A. Kahn-Harari, and B. Viana, Synthesis and optical characterization of $SrHfO_3$: Ce and $SrZrO_3$: Ce nanoparticles, Opt. Mater. 30, 1109-1114 (2008).
[98] T. Noguchi, T. Okubo, and O.Yonemochi, Reactions in the System $ZrO_2$:SrO, J. Am. Ceram. Soc. 52, 178 (1969).
[99] J. K. Gleason, H. W. Olsen, and W. D. Turley, Pressure-induced luminescence quenching of terbium-doped oxide sulfides, Inorg. Chem. 32, 639 (1993).
[100] H. E. Hoefdraad, The charge-transfer absorption band of $Eu^{3+}$ in oxides, J. Solid State Chem. 15, 175 (1975).
[101] H. Yamamoto, M. Mikami, Y. Shimomura, and Y. Oguri, Host-to-activator energy transfer in a new blue-emitting phosphor $SrHfO_3$: $Tm^{3+}$, J. Lumin. 87, 1079-1082 (2000).
[102] A. Dobrowolska and E. Zych, Forcing $Eu^{3+}$ into Different Positions in the $BaHfO_3$ Host and Its Spectroscopic Consequences, Chem. Mater. 22, 4652-4659 (2010).
[103] S. K. Gupta, M. Mohapatra, V. Natarajan, and S.

V. Godbole, Site-specific luminescence of $Eu^{3+}$ in gel-combustion-derived strontium zirconate perovskite nanophosphors, J. Mater. Sci. 47, 3504-3515 (2012).

[104] S. Liu, X. Feng, Z. Zhou, M. Nikl, Y. Shi, and Y. Pan, Effect of $Mg^{2+}$ co-doping on the scintillation performance of LuAG:Ce ceramics, Phys. Status Solidi 8, 105-109 (2014).

[105] M. Nikl, V. Babin, J. Pejchal, V. V. Laguta, M. Buryi, J. A. Mares, K. Kamada, S. Kurosawa, A. Yoshikawa, D. Panek and T. Parkman, The Stable $Ce^{4+}$ Center: A New Tool to Optimize Ce-Doped Oxide Scintillators, IEEE Trans. Nucl. Sci. 63, 433 (2016).

[106] W. Chepraditkul, C. Wanarak, T. Szczesniak, M. Moszynski, V. Jary, A. Beitlerova, and M. Nikl, Comparison of absorption, luminescence and scintillation characteristics in Lu1.95Y0.05SiO5:Ce, Ca and Y2SiO5:Ce scintillators, Opt. Mater., 35, 1679-1684, (2013).

[107] R. A. Davies, M. S. Islam, and J. D. Gale, Dopant and proton incorporation in perovskite-type zirconates, Solid State Ion. 126, 323-335 (1999).

[108] F. A. Kröger and H. J. Vink, Solid State Physics – Advances in Research and Applications (Academic Press, New York, 1957).

[109] See Supplemental Material at [URL to be inserted by publisher] for total and partial (Ce $4f$ and $5d$) density of states for the two most stable Ce substitutional doping configurations in $CaZrO_3$, $SrHfO_3$, $SrZrO_3$, $BaHfO_3$ and $BaZrO_3$.